



# A CPFD Simulation on Hydrodynamics of Carbon Nanotube Aggregates in a Fluidized Bed

Suyoung Kim<sup>1</sup> · Min Ji Lee<sup>2</sup> · Ye Ji Chang<sup>2</sup> · Yujin Go<sup>2</sup> · Geunhye Won<sup>2</sup> · Sung Won Kim<sup>1,2</sup>

Received: 7 June 2024 / Revised: 4 August 2024 / Accepted: 11 August 2024  
© The Author(s), under exclusive licence to Korean Institute of Chemical Engineers, Seoul, Korea 2024

## Abstract

A computational particle–fluid dynamics (CPFD) model of a fluidized bed reactor with carbon nanotube (CNT,  $d_p = 485 \mu\text{m}$ ) particles was established. A drag model and coefficient were determined to simulate the hydrodynamic behavior of CNTs in a fluidized bed. The drag coefficient reflected the variation in physical properties owing to CNT agglomeration, such as aggregate size distribution, particle circularity, and apparent density. The Richardson–Davidson–Harrison model with a drag coefficient of 0.17 was chosen based on results on solid holdup distribution. The proposed CPFD model described hydrodynamic behaviors, such as bed expansion, solid holdup distribution, and relative standard deviation (RSD) of the pressure drop with gas velocity, and predicted the transition gas velocity between the partial and complete fluidization regimes. The bed expansion and RSD gradually increased with increasing gas velocity in the partial fluidization regime and rapidly increased at the beginning of the complete fluidization regime. The increased gas velocity significantly enhanced bed expansion and particle entrainment, resulting in the formation of large CNT aggregates and a higher solid holdup in the freeboard in the complete fluidization regime. The simulated results describe the behavior of CNT aggregates near the bed surface and in the freeboard region, supporting previous findings in the literature. Uneven local gas flows occurred in the bed and freeboard regions, and the results described the bubbling bed characteristics in the complete fluidization regime.

**Keywords** Carbon nanotube · Fluidized bed · Simulation · CNT aggregates · Particle behavior

## List of symbols

$C_D$	Drag model coefficient
$d_p$	Mean particle diameter [m]
$D_p$	Aerodynamic drag function
$f$	Particle size distribution function
$F$	Momentum transfer between the fluid and solid phases
$g$	Gravity acceleration [ $\text{m/s}^2$ ]
$m$	Mass [kg]
$p$	Pressure [Pa]
$P_s$	Positive constant for particle normal stress [Pa]
$Re$	Reynold number
$T$	Temperature [K]

$t$	Time [s]
$u$	Velocity [m/s]
$X$	Contact-stress acceleration [ $\text{m/s}^2$ ]

## Greek symbols

$\alpha$	Volume fraction
$\beta$	Constant
$\varepsilon$	Constant
$\varepsilon_s$	Solid holdup or solid volume fraction
$\delta_{ij}$	Kronecker delta
$\mu$	Viscosity [kg/ms]
$\rho$	Density [ $\text{kg/m}^3$ ]
$\tau_p$	Particle normal stress [Pa]
$\tau_g$	Gas stress tensor [Pa]
$\tau_D$	Collision damping time [s]
$\omega$	Particle sphericity

## Subscripts

$cp$	Close pack
$eff$	Effective viscosity
$f$	Fluid
$i, j, k$	Coordinate index
$p$	Particle
$s$	Solid

✉ Sung Won Kim  
kswcfb@ut.ac.kr

<sup>1</sup> Department of IT·Energy Convergence, Korea National University of Transportation, Chungju-Si 27469, Chungbuk, Korea

<sup>2</sup> Department of Chemical and Biological Engineering, Korea National University of Transportation, Chungju-Si 27469, Chungbuk, Korea

## Introduction

Carbon nanotubes (CNTs) have been extensively used in various fields as battery electrode additives, high strength fibers, and heat transfer enhancers, owing to their excellent mechanical, electrical, and thermal properties [1–3]. The most prevalent methods for CNT synthesis are electric arc discharge, laser ablation, plasma-based synthesis, and catalytic chemical vapor deposition (CCVD). Among these methods, CCVD can achieve economical mass production [1, 4]. In particular, the fluidized bed-based catalytic chemical vapor deposition (FBCVD) technique is known to be appropriate for the large-scale CNT synthesis because of its advantages, including a high particle mixing ratio and efficient heat and mass transfer rate, as well as the large specific surface area of the catalytic reaction [1, 4].

CNT growth on a catalyst causes an increase in particle size, a rapid drop in density, and particle agglomeration by entanglement between the nanotubes [5]. Particle agglomeration is caused by the strong interaction of van der Waals forces during fluidization [6, 7]. Handling CNT powder in a fluidized bed reactor is difficult owing to rapid changes in their physical properties with aggregation. Studies on the hydrodynamic behavior based on the characterization of CNT aggregates are required for reactor design, scale-up, and optimization of operation [7].

Numerous investigations have explored the hydrodynamic behavior of CNT aggregates in fluidized beds [6–9]. Wang et al. [8] reported that CNT agglomerates behaved similarly to Geldart A particles with increasing gas velocity. Yu et al. [6] reported the formation of multi-staged agglomerate structures of multi-walled carbon nanotubes (MWCNTs) and their high bed expansion ratio in a fluidized bed owing to the porous structure of CNT aggregates. Kim [9] analyzed the mechanism of CNT agglomerate formation in the freeboard region by measuring the aggregate size via visualization using a laser sheet technique. The studies concluded that CNT exist mainly in the form of aggregates in the complete fluidization regime, and that the hydrodynamic behavior of CNTs, not only in the dense bed but also in the freeboard, is governed by CNT aggregates, indicating that the aggregate characteristics should be reflected in the dynamic modeling of a fluidized bed reactor of CNT.

Numerous efforts have been made to simulate the behavior of aggregates or particle clusters in fluidized beds [10, 11]. Drag correlations are crucial for simulating particle clustering [10], because a grouped cluster of particles experiences a decrease in the drag coefficient by increasing the gas flow around the clusters and decreasing their penetration [11]. Therefore, modifying existing drag models and adjusting the drag coefficient is necessary to accurately simulate the behavior of CNT agglomerates.

In recent decades, modeling and simulation have become crucial tools in the design, optimization, and scale-up of fluidization systems [12]. Computational simulation approaches have been used as auxiliary methods for the analysis of complex particle behavior, which is difficult to access experimentally in gas–solid fluidized beds. Recently, the multiphase particle-in-cell (MP-PIC) method, specifically developed for computational particle fluid dynamics (CPFD) simulations, has been applied as an efficient method for simulating large-scale particle systems, with considerable savings in time and technical and economic resources [13]. Therefore, this approach will be useful for reactor design and the determination of reaction conditions with the ability to easily predict changes in CNT behavior owing to structural and scale modifications within the reactor.

In this study, a CPFD simulation was conducted using the MP-PIC model, and a drag model with controlled coefficients was proposed to simulate the behavior of CNTs in a fluidized bed. The experimental data from Lee and Kim [14] and Lee et al. [3] were used to verify the model. The hydrodynamic characteristics of CNTs in a fluidized bed, such as the bed expansion and axial solid holdup distribution, were simulated using the proposed drag model with a controlled drag coefficient.

## Mathematical Models

### Governing Equations

Barracuda Virtual Reactor 22.0.0 software base on the MP-PIC approach was used for the analysis of CNT behavior in a fluidized bed. The MP-PIC model uses the Lagrangian approach for the particle phase, whereas the Eulerian approach or Eulerian–Lagrangian method applies continuity equations to the gas phase. This model is advantageous for reducing the calculation time for fluidized bed process analysis with complex particle behavior using a particle distribution function to track the movement of particle groups [15].

In the MP-PIC model, the governing and momentum equations used to analyze the behavior of fluids and solids are as follows [16–19]:

Continuity equation:

$$\frac{\partial(\alpha_g \rho_g)}{\partial t} + \nabla \cdot (\alpha_g \rho_g u_g) = 0, \quad (1)$$

where  $\alpha_g$ ,  $\rho_g$ ,  $u_g$  are the gas volume fraction, density and velocity vector, respectively.

Momentum conservation equation: (2)

$$\frac{\partial(\alpha_g \rho_g u_g)}{\partial t} + \nabla \cdot (\alpha_g \rho_g u_g u_g) = -\nabla p + F + \alpha_g \rho_g g + \nabla \cdot \tau_g,$$

where  $p$ ,  $g$ ,  $F$  are pressure, gravitational acceleration, and the momentum exchange rate between the gas and solid phases, respectively.  $\tau_g$  is the gas stress tensor, represented as follows:

$$\tau_g = \mu_{\text{eff}} \left( \frac{\partial u_{g,i}}{\partial X_j} + \frac{\partial u_{g,j}}{\partial X_i} \right) - \frac{2}{3} \mu_{\text{eff}} \delta_{ij} \frac{\partial u_k}{\partial X_k}, \tag{3}$$

where  $\delta_{ij}$  is the Kronecker delta, and  $\mu_{\text{eff}}$  is the gas effective viscosity that consists of two components, namely, laminar and turbulence.

The distribution of particles in space is depicted by the probability distribution function ( $f$ ). In numerical simulations, the particle phase is modeled as discrete particles, each of which contains several real particles with the identical volume, density, velocity, and position [20, 21].

The particle equation of motion is expressed as follows:

$$\frac{du_p}{dt} = D_p(u_g - u_p) - \frac{\nabla p}{\rho_p} + X + g + \frac{\bar{u}_p - u_p}{2\tau_D}, \tag{4}$$

$$X = -\frac{1}{\rho_p \alpha_s} \frac{\partial \tau_p}{\partial X_i} + g_1(\alpha_s) \left[ \bar{D}(u_g - \bar{u}_p) - D(u_g - \bar{u}_p) - \left( \frac{1}{\rho_p} - \frac{1}{\rho_p} \right) \frac{\partial p}{\partial X_i} \right], \tag{5}$$

$$\tau_p = \frac{10P_s \alpha_p^\beta}{\max[(\alpha_{cp} - \alpha_p), \epsilon(1 - \alpha_p)]}, \tag{6}$$

$$g_1(\alpha_s) = \begin{cases} 0 & \text{if } \alpha_s = 0 \\ 1 & \text{if } \alpha_s = \alpha_{s,cp} \end{cases}, \tag{7}$$

$$\bar{D} = \frac{\int \int \int f m D d m_p d u_p d T_p}{\bar{\rho}_p \alpha_s}, \tag{8}$$

$$\bar{u}_p = \frac{\int \int \int f m D u_p d m_p d u_p d T_p}{\bar{\rho}_p \alpha_s \bar{D}}, \tag{9}$$

where  $D_p$ ,  $\rho_p$ ,  $\bar{u}_p$ ,  $\tau_p$ ,  $X$  are the interphase drag coefficient, the particle density, the cell-averaged particle velocity, the collision damping time, and the contact–stress acceleration, respectively. The particle normal stress  $\tau_p$  is used to describe the particle–particle interactions.

### Drag Models

The drag force model has a substantial influence on the simulation results of the hydrodynamics of CNT agglomerates

in a fluidized bed. Numerous studies have demonstrated that the drag force model significantly influences the concentration distribution of solids, solid velocities, and particle clusters [12, 22, 23].

The interphase momentum transfer term  $F$  in Eq. (2) is expressed by Eqs. (10) as follows:

$$F = \int \int \int f \left\{ m_p \left[ D_p(u_g - u_p) - \frac{\nabla p}{\rho_p} \right] + u_p \frac{dm_p}{dt} \right\} d m_p d u_p d T_p, \tag{10}$$

where  $m_p$  is the parcel mass.

The drag force model of the gas–solid phase was employed to characterize their interaction, which constitutes a significant portion of the particle forces. In this study, drag models, such as the WenYu–Ergun [24], Richardson–Davidson–Harrison [25], and non-spherical Ganser models [25], were evaluated to simulate the fluidization behavior of CNT aggregates. The correlations are presented in Table 1 [24–28]. The WenYu–Ergun drag model combines the WenYu [27] and Ergun [28] methods, enabling the description of particle behavior in both dilute and dense phases. Richardson–Davidson–Harrison drag model [25] was devised to investigate the bubble behavior in gas–solid fluidized beds [29] and is based on the Wen-Yu drag model, while omitting the effect of the particle volume fraction [30]. For non-spherical particles, the Ganser correlation showed the most accurate prediction of the particle cluster drag coefficient [26].

**Table 1** Drag models used in CPF D simulations

WenYu–Ergun model [24]

$$D_p = \begin{cases} D_1 = \frac{6}{8} C_D \frac{\rho_g |u_g - u_p|}{\rho_p d_p}, \alpha_s < 0.75 \alpha_{s,cp} \\ \frac{\alpha_s - 0.85 \alpha_{s,cp}}{0.85 \alpha_{s,cp} - 0.75 \alpha_{s,cp}} (D_2 - D_1) + D_1, 0.75 \alpha_{s,cp} \leq \alpha_s < 0.85 \alpha_{s,cp} \\ D_2 = \left( \frac{180 \alpha_s}{\alpha_g \text{Re}} + 2 \right) \frac{\rho_g |u_g - u_p|}{\rho_p d_p}, \alpha_s > 0.85 \alpha_{s,cp} \end{cases}$$

$$D_p = \frac{6}{8} C_D \frac{\rho_g |u_g - u_p|}{\rho_p d_p}$$

Richardson–Davidson–Harrison model [25]

$$C_D = \frac{24}{\text{Re}} (1 + 0.15 \text{Re}^{0.681}) + \frac{0.407}{1 + \frac{8710}{\text{Re}}}$$

Non-spherical Ganser model [26]

$$C_D = \alpha_s^{-2.65} K_2 \left[ \frac{24}{\text{Re} K_1 K_2} (1 + 0.1118 (\text{Re} K_1 K_2)^{0.6567}) + \frac{0.4305}{1 + \frac{3305}{\text{Re} K_1 K_2}} \right]$$

$$K_1 = \frac{3}{1 + 2\omega^{-0.5}}, K_2 = 10^{1.8148(-\log \omega)^{0.5743}}$$

## Simulated Conditions

The simulation was based on the experimental studies of hydrodynamics in a CNT-fluidized bed conducted by Lee and Kim [14] and Lee et al. [3]. The experimental apparatus consists of a tuyere gas distributor (4 mm—hole diameter; hole number = 20) and a main column (0.15 m i.d. by 2.6 m height) with cyclone as shown in Fig. 1a. The CPFD model simulated particles behavior in the reactor part to evaluate the drag model through the validation of the solid holdup distributions in the main column and the local particle behavior in the freeboard, as illustrated in Fig. 1b. A cyclone in Fig. 1a was not included in the simulation considering that almost no aggregated particles are emitted from the expanded column of reactor [14].

The total number of cells was 16,546, and the grids were sufficient for the simulation. The grid size and cell number of this model are optimized values from the simulation performed of fluidized bed reactor in previous study [19]. The simulation results were calculated for 60 s. The simulated results for a period between 20 and 60 s were post-processed for the analysis of particle behavior because the fluidized operation reached the steady state after 20 s with obtaining a balance between inlet and outlet gas flow rates [17, 19].

The solid particles used in this study were multi-walled CNTs, which are recognized for their long, dense, and well-ordered bundles of nanotubes. The MWCNTs are identical to those employed in previous studies [3, 14]. The

characteristic leads to a distinctive appearance in which the nanotubes grown from different particles are physically interwoven, as shown in Fig. 2a [31]. Handling CNT particles in a fluidized bed reactor is problematic because the cohesive force between the particles is greater than the hydrodynamic force exerted by the fluid phase [32]. The formation of CNT aggregates is unavoidable in fluidized beds. The CNT particles in the fluidized bed exhibited aggregated shapes, as shown in Fig. 2b. The primary formation of aggregates was caused by the physical entanglement of nanotubes on different CNT particles. Secondary aggregates are formed by the sticking of nanotubes to primary aggregates via van der Waals forces [7, 9]. With an increase in the aggregate size formed by cohesion, the internal porosity and specific surface area of the aggregates increased, resulting in a decrease in particle density. The physical properties of the CNT agglomeration were applied to the CPFD simulation to improve simulation accuracy. The particle circularity and apparent density for the simulation were obtained using an imaging method on the enveloped volume of entangled CNT particles [14]. The particle size distributions of the CNT agglomerations with the gas velocity were measured using the laser sheet technique of Kim [7], as shown in Fig. 2c. The fixed bed height was 0.82 m with a volume fraction of 0.61; other input parameters are listed in Table 2.

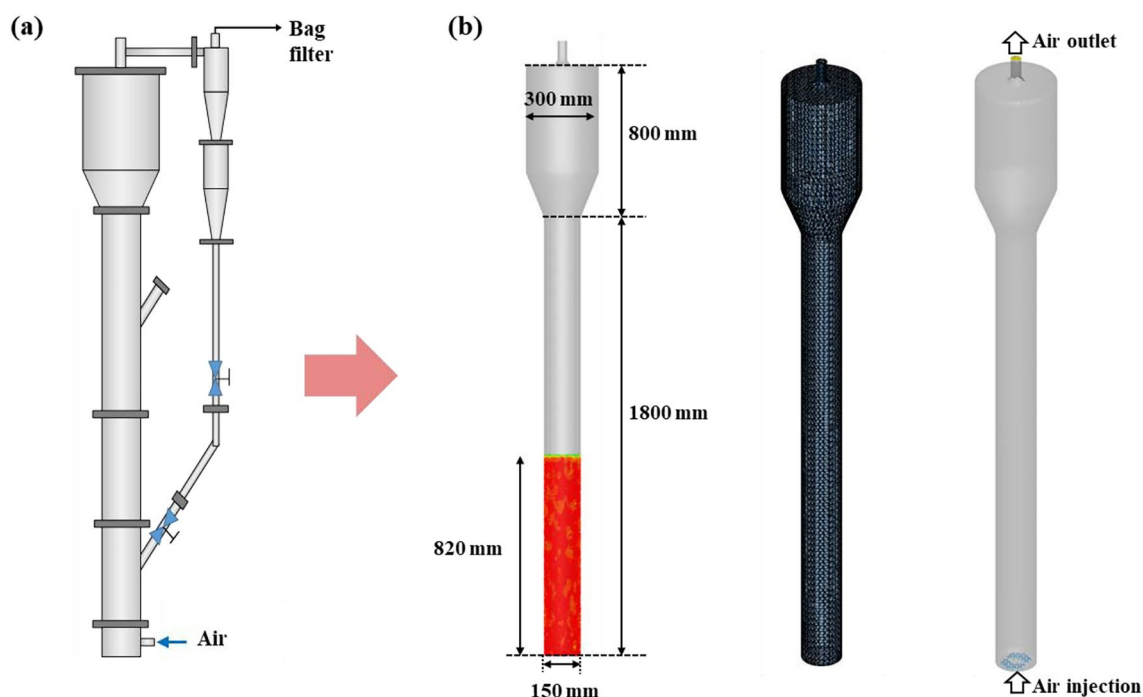


**Fig. 1** Experimental apparatus used for **a** cold model and **b** simulation

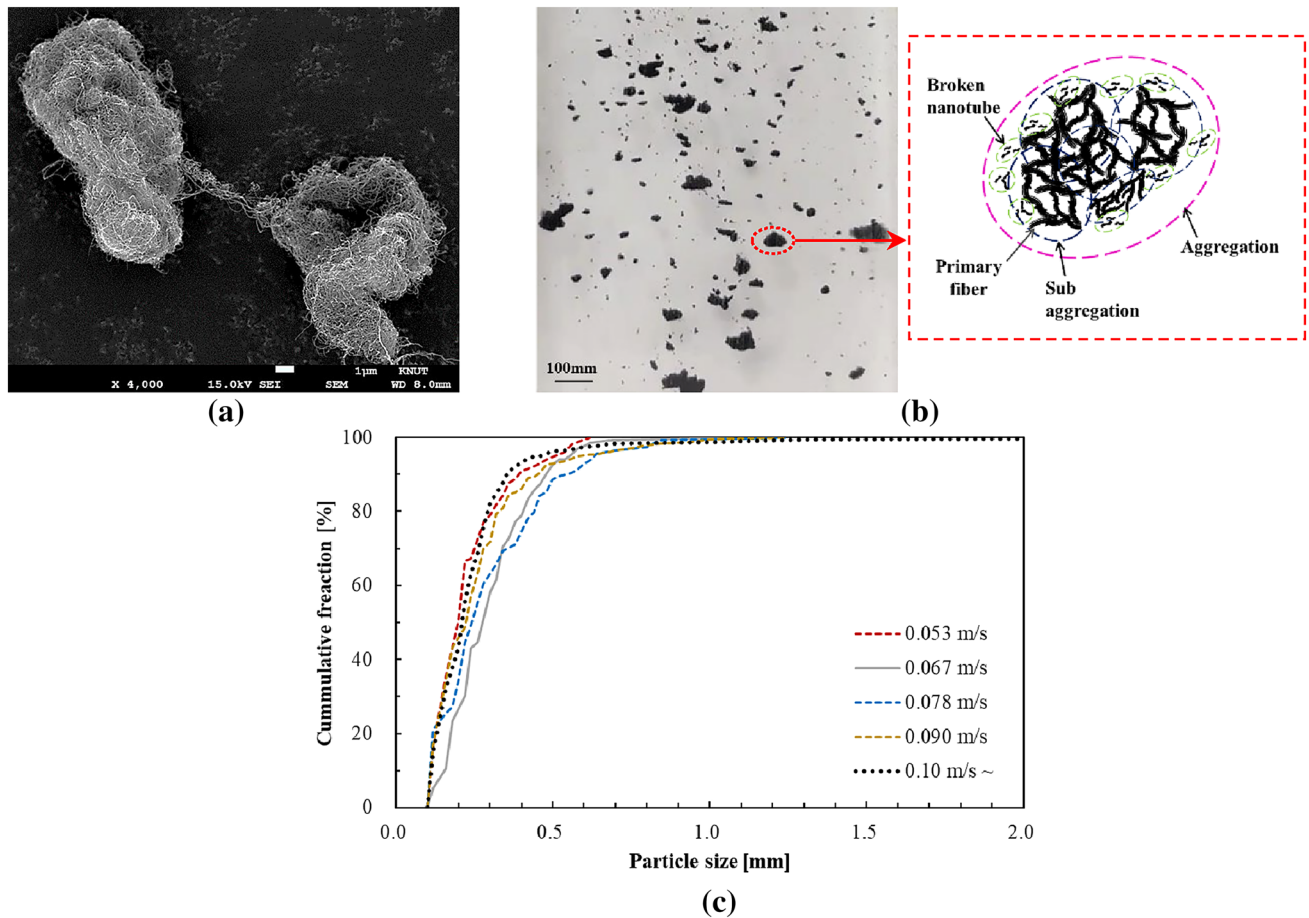


**Fig. 2** **a** SEM image of MWCNT, **b** CNT aggregates in a sedimentation column, and **c** size distribution of MWCNT particles used in simulation

**Table 2** Input parameters used in CPFD simulation

Parameters	Numerical value	References
MWCNT bulk density	19 kg/m <sup>3</sup>	[14]
MWCNT particle density	31 kg/m <sup>3</sup>	[14]
Transition velocity between flow regimes of fixed bed and partial fluidization	0.0019 m/s	[3]
Transition velocity between flow regimes of partial fluidization and complete fluidization	0.10 m/s	[3]
Gas velocity	0.05–0.19 m/s	
Gas composition	Air	
Sphericity	0.71	
Initial bed height	0.82 m	
Total number of all cells	48,300	
Total number of real cells	16,456	
Time step	0.001 s	
Simulation time	60 s	

## Result and Discussion

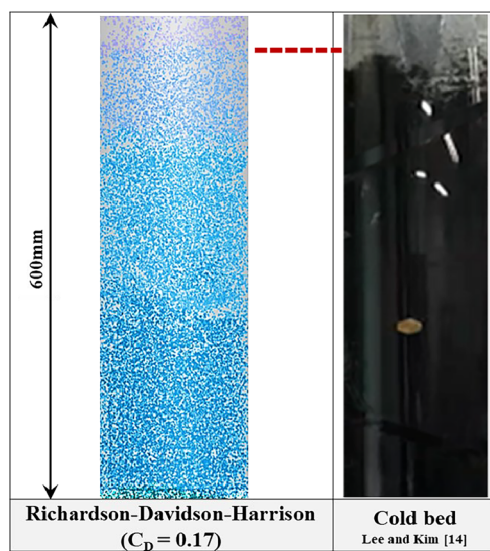
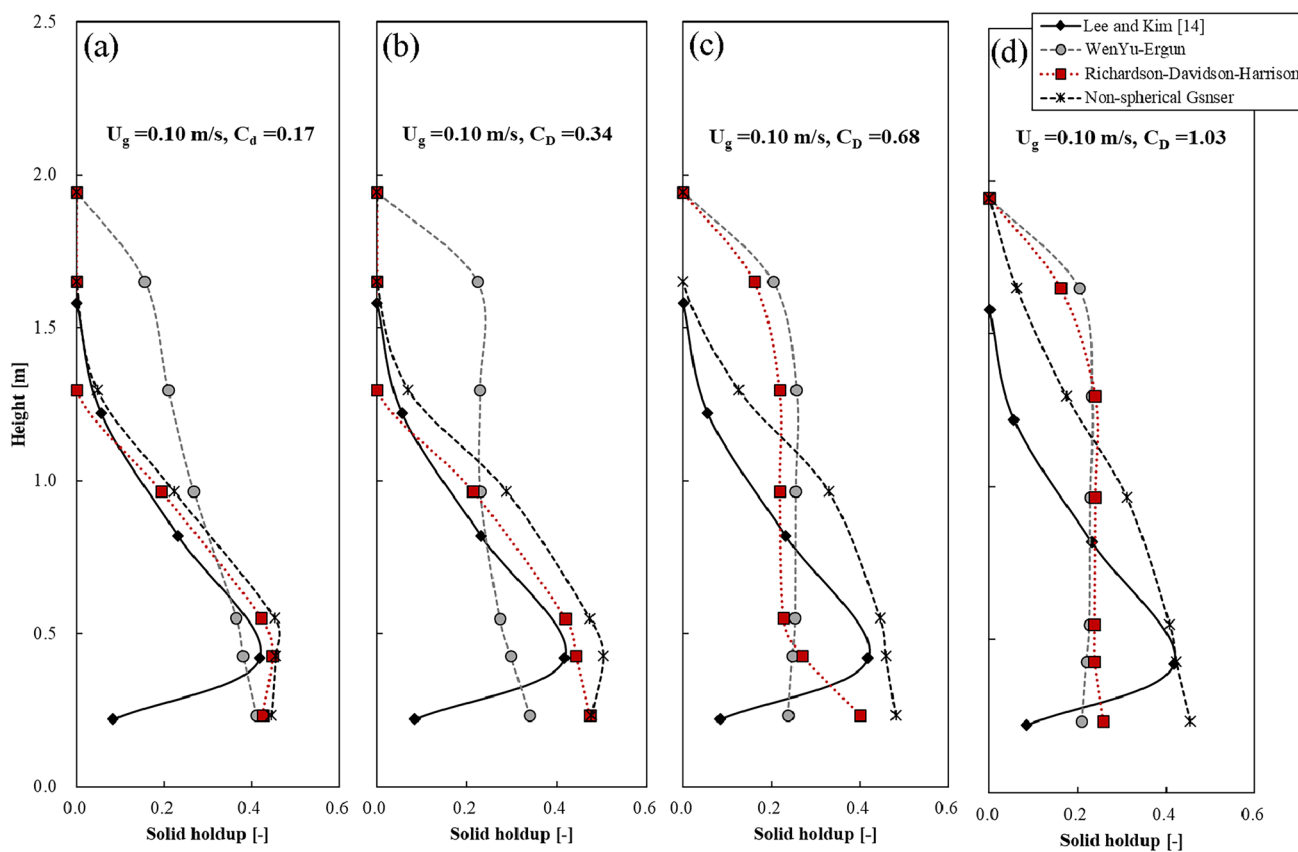
### Axial Solid Holdup Distribution

Figure 3 shows the simulated results for the axial solid holdup distributions obtained from different drag models and coefficients at gas velocity ( $U_g$ ) of 0.10 m/s. The simulation was conducted using drag models and correction factors of the coefficient, which were dominated by the behavior of the CNT aggregates. The solid holdup ( $\epsilon_s$ ) values in the reactor were calculated by Eq. (11) from the pressure drops along the height ( $\Delta P/\Delta L$ ), obtained from the pressure profile in the simulation, postulating that the effects of gas acceleration and wall fraction were disregarded [33].

$$\epsilon_s = \frac{\Delta P}{\Delta L} / [(\rho_s - \rho_g)g], \tag{11}$$

where  $\rho_g$  and  $\rho_s$  are gas and particle density, respectively,

The CNTs agglomeration with the growth of nanotubes indicated that their densities decreased, and the enveloped volumes (Fig. 2b) increased with an increase in the inner



**Fig. 3** Axial solid holdup distributions by drag coefficient:  $C_D=0.17$  (a), 0.34 (b), 0.68 (c), 1.03 (d); (e) upper part of CNT fluidized bed at  $U_g=0.10\text{m/s}$

voidage in the CNT aggregate. The drag coefficient in the model reflects the variation in the effective projected area of the aggregates. The drag coefficient was varied from 0.17 to 1.03 by adjusting the respective model multipliers of the

drag force. To accurately reflect the aggregate morphology within the reactor, the drag force conditions were selected by comparing the average axial solid holdup distribution with the experimental results of Lee and Kim [14]. The

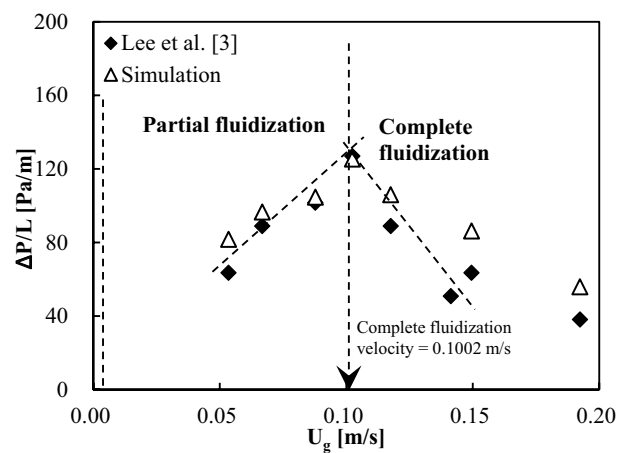
bed height increased with the drag coefficient owing to the increased drag force on the CNT aggregates. The experimental results revealed that the solid holdup distribution exhibited an S-shape, consisting of a lower-density phase at the bottom, a transitional region in the middle, and a dilute phase at the top, as observed in a typical bubbling fluidized bed [7]. The axial solid holdup distributions obtained from the Richardson-Davidson-Harrison model with a 0.17 drag coefficient were matched well with the experimental S-shaped curves at 0.1 m/s.

The simulated bed expansion behavior is similar to the particle behavior observed near the bed surface, as shown in Fig. 3e. The experimental results were based only on the average value of the  $\varepsilon_s$  within the bed, and it was difficult to approach the local value variation. The simulation results indicated that the  $\varepsilon_s$  in the bed decreased with increasing height, and the  $\varepsilon_s$  near the bed surface was lower than that near the distributor. This suggests that intensified agglomeration of the CNT powder leads to a high presence of low-density CNT aggregates in the upper region of the bed. These findings align well with the results of Kim and Kim [34], who reported that a significant portion of the elutriated CNT particles existed in the form of aggregates on the freeboard.

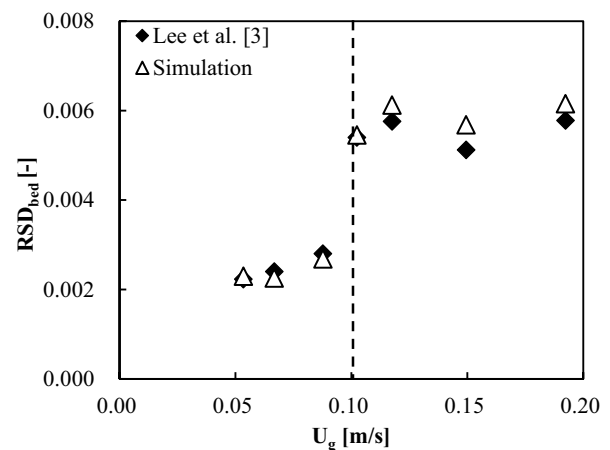
### Flow Regimes Transition

Figure 4a shows the effect of gas velocity on  $\Delta P/\Delta L$  to identify the flow regime transition in the CNTs bed. The flow regime of the CNT powder is transition from a fixed bed to complete fluidization regimes with gas velocity ( $U_g$ ) [35]. The  $\Delta P/\Delta L$  increased with  $U_g$  in the partial fluidization regime, resembling the bed behavior of the cohesive Geldart C group. The intensified agglomeration or network formation of CNTs in this regime results in gas channels in the bed. With an increase in  $U_g$ , local fluidization occurs with the gradual collapse of the bed in the vicinity of the enlarged gas channel [3, 35].  $\Delta P/\Delta L$  reaches its maximum value at  $U_g = 0.10$  m/s, signifying a transition to the complete fluidization regime.  $\Delta P/\Delta L$  decreases with  $U_g$ , similar to a typical bed of Geldart A or B particles. The simulated results of the change in  $\Delta P/\Delta L$  with  $U_g$  are presented and compared in Fig. 4a. The model accurately described the experimental results, indicating that the regime transition of the CNT bed was governed by particle aggregation. The relative standard deviation (RSD) of the pressure fluctuations, calculated using Eq. (12–14), was employed to characterize the gas–solid behavior in the bed [36, 37].

$$\text{Standard deviation, } \sigma = \sqrt{\frac{1}{N-1} \sum_{n=1}^N (x(n) - \bar{x})^2}, \quad (12)$$



(a)



(b)

Fig. 4 Effect of gas velocity on solid holdup (a) and RSD (b) of bed

$$\bar{x} = \frac{1}{N} \sum_{n=1}^N x(n), \quad (13)$$

where  $N, x(n), \bar{x}$  are the overall measurement time and the pressure drop at the measurement time and the averaged pressure drop, respectively. The RSD was obtained using Eq. (14) [37].

$$\text{RSD} = \sigma / \Delta \bar{P}, \quad (14)$$

Figure 4b shows the effect of  $U_g$  on the RSD of the pressure drop in the bed. The RSD was constant in the partial fluidization regime, because the bed region, other than the channel, stagnated after the formation of gas channels [3]. However, the RSD increased abruptly after 0.10 m/s, when the gas channels collapsed and the bed was under entirely active movement in the complete fluidization regime. The model satisfactorily simulated the variation in the RSD

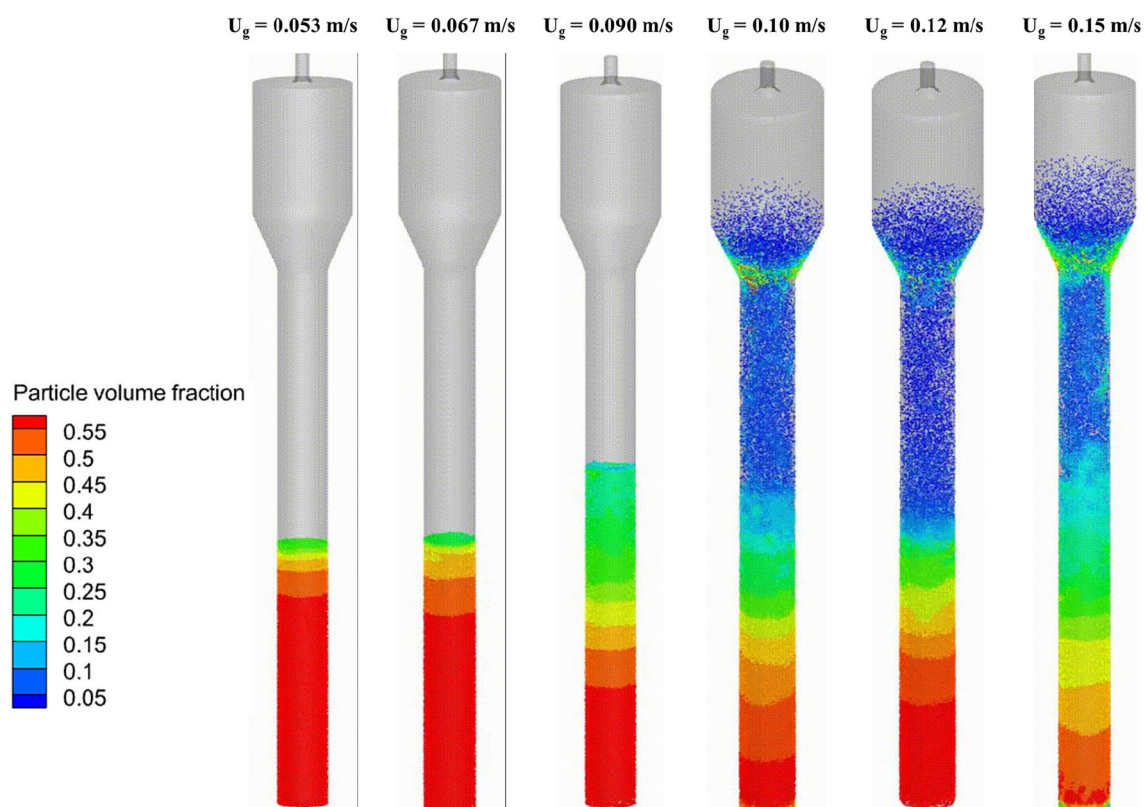


Fig. 5 Effect of gas velocity on particle volume fraction in the reactor (time = 60 s)

with  $U_g$ , indicating that the proposed drag model accurately described the CNT bed behavior.

### Bed Expansion Behavior

The simulated bed expansion and local particle volume fraction at different dimensionless heights with the gas velocity are shown in Figs. 5 and 6, respectively. In Fig. 6, the dimensionless height is defined as a bed height divided by reactor height. The particle volume fraction did not change with height up to 0.067 m/s in the partial-fluidization regime. With a further increase in  $U_g$  (0.090 m/s), the solid holdup ( $\epsilon_s$ ) below the bed surface decreased owing to bed expansion by the enlarged gas channels and local fluidization of the bed [3, 35]. An increased  $\epsilon_s$  above the bed surface was observed because of the increase in particle entrainment through the gas channels [3]. However, this fraction appeared to be uniformly distributed throughout the simulation. The simulated results did not match well with the experimental results of Lee and Kim [14] and Lee et al. [3] because the model was limited in describing occurrence of the gas channels. The

bed expansion rapidly increased after 0.10 m/s, which is the beginning of the complete fluidization regime. In this regime, the drag force of the gas exceeded the cohesive force between the CNT particles. In the dilute phase of the freeboard, the  $\epsilon_s$  increased because of the increase in particle entrainment caused by the increased  $U_g$ . These results support the variation in the RSD of the  $\Delta P$  in the bed with  $U_g$ , as shown in Fig. 4b.

Figure 7 shows the simulated results of the particle behavior near the bed surface and on the freeboard with the  $U_g$ . In the partial-fluidization regime, no particle elutriation was observed within the freeboard. However, in complete fluidization, the  $\epsilon_s$  of the freeboard increased with  $U_g$  because of the increased number of CNT aggregates formed by particle elutriation. The formation of agglomerate in the dilute phase is due to the physical entanglement of nanotubes, which are detached from the particles owing to interparticle collisions in the dense bed with CNT particles or agglomerates [38]. In the complete fluidization regime, the activity at the bed surface increased with  $U_g$ , and a large entrainment of CNTs



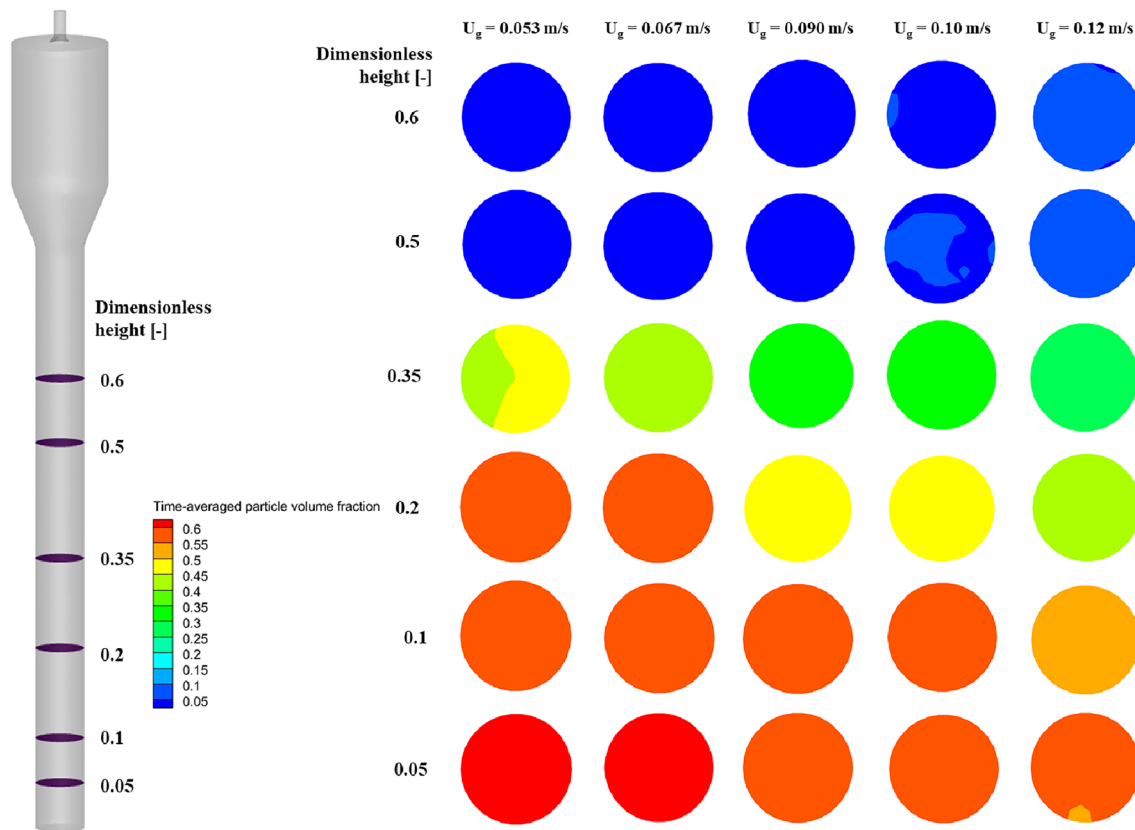


**Fig. 6** Particle volume fraction at different heights in the reactor with gas velocity

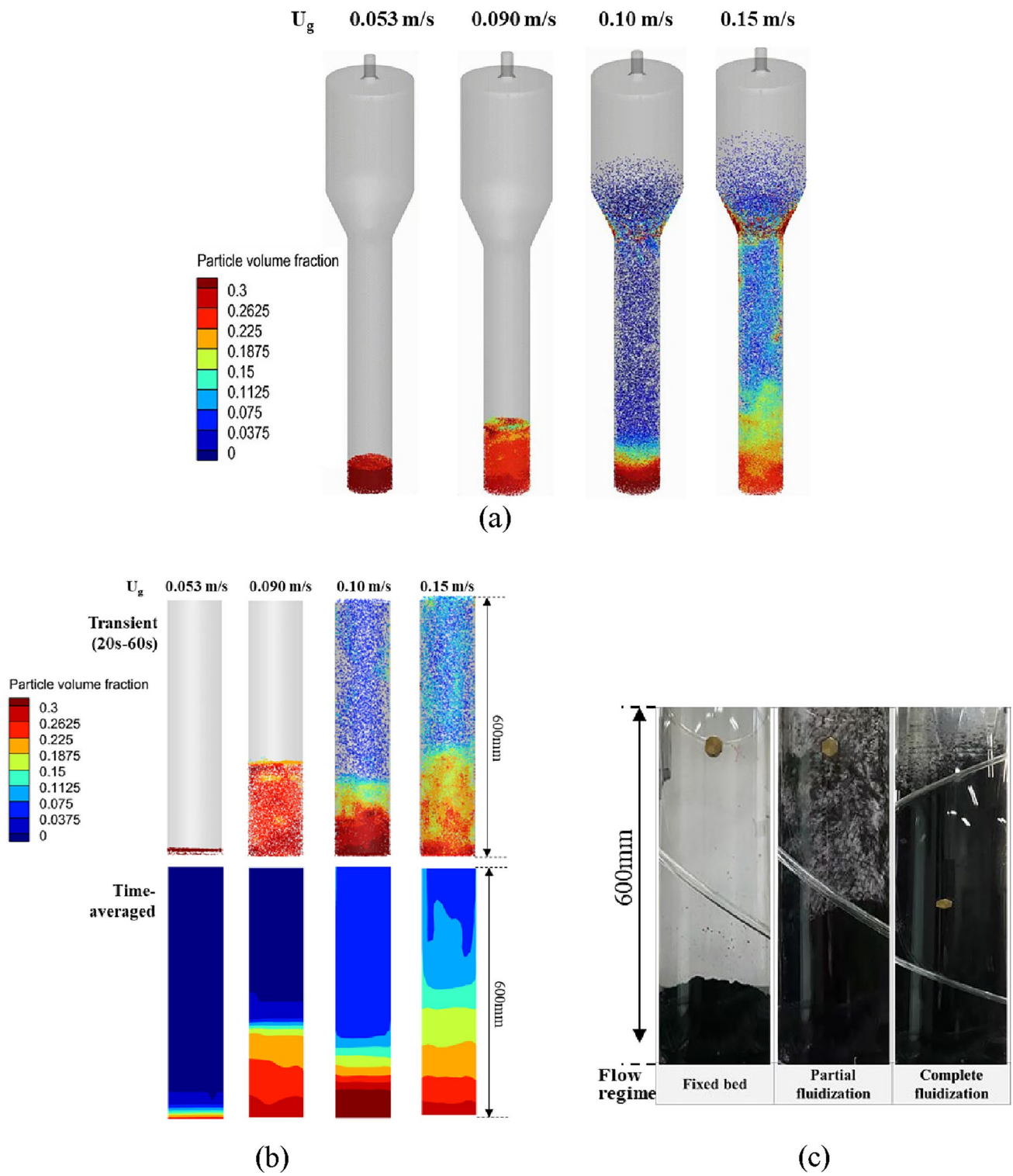
occurred owing to the increased drag force due to the increased projected area of particle agglomerates. The bed surface behavior was similar to that observed at the same height in the cold bed (Fig. 7c) in the complete fluidization regime. However, the nonuniform elutriated behavior of the aggregates from the bed surface (Fig. 7c) was not simulated in the partial fluidization regime for the same reason mentioned in the discussion of Fig. 5. Further studies are required to simulate the gas channels in the bed and the detailed behavior of CNTs during partial fluidization.

Figure 8 shows the simulated results for the local gas velocity in a reactor with superficial gas velocity. The gas velocity ( $U_g$ ) of the bed gradually increased with the superficial gas velocity in the partial fluidization regime. In partial fluidization, an uneven local gas velocity was observed at  $U_g = 0.053$  m/s, partially revealing the gas-channelling phenomena. However, channelling did not develop above 0.067 m/s, unlike the observations from the experiments. Local gas velocity in bed increased after  $U_g = 0.1$  m/s, showing increased bubble frequency and bubble size in bed. The local gas velocities in the

freeboard increased with  $U_g$ , and nonuniform distributions were observed because of the increased fluctuation of the bed surface and entrainment of the CNT aggregates. These results support the variation in the RSD of  $\Delta P$  in the bed with  $U_g$  (Fig. 4). Finally, the simulation results describe the flow regime transitions and local particle dynamics in the complete fluidization regime with  $U_g$ .

## Conclusion

The drag model and coefficient were determined to simulate the hydrodynamic behavior of the CNTs in a fluidized bed of MWCNTs. The Richardson-Davidson-Harrison model with a drag coefficient of 0.17 was chosen based on a comparison of the experimental results for the solid holdup distribution. The proposed CPFD model simulated well bed expansion, solid holdup distribution, and RSD with  $U_g$ , and predicted the transition  $U_g$  between the partial and complete fluidization regimes. The bed expansion



**Fig. 7** Particle volume fraction around bed surface with gas velocity in simulation (a), (b), and bed flow phenomena in cold bed (c)

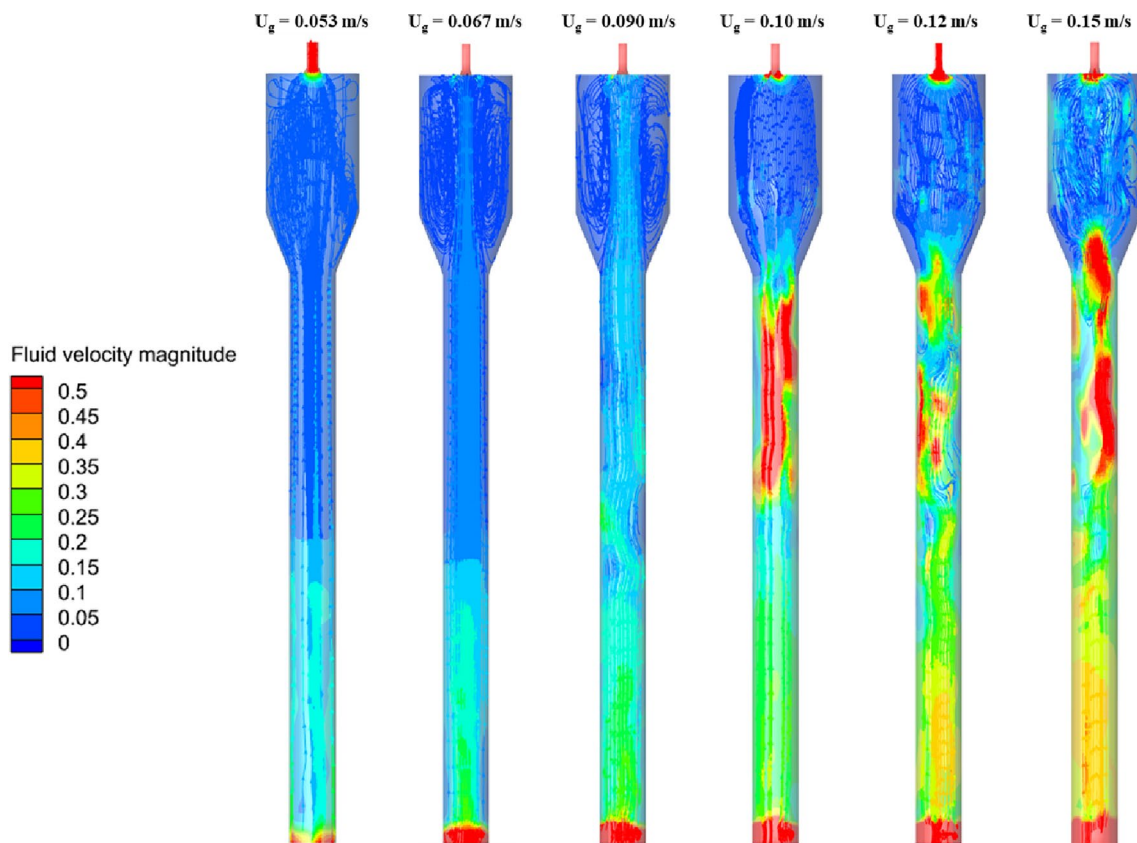


**Fig. 8** Effect of superficial gas velocity on local gas velocity in the reactor (time = 60 s)

and RSD of  $\Delta P/\Delta L$  gradually increased with increasing  $U_g$  in the partial fluidization regime and rapidly increased at the beginning of the complete fluidization regime. Increased  $U_g$  significantly enhanced bed expansion and particle entrainment in the complete fluidization regime, resulting in the formation of large CNT aggregates and a higher  $\epsilon_s$  in the freeboard. The simulated behavior was similar to observations in the cold bed but limited to the description of nonuniform aggregate elutriation in partial fluidization. The simulated results describe the behavior of CNT aggregates near the bed surface and in the freeboard region, supporting previous findings in the literature. Uneven local gas flow occurred in the bed and freeboard regions, and the results describe the bubbling bed characteristics in the complete fluidization regime of the CNT fluidized bed.

**Acknowledgements** This work was supported by the Korea Planning & Evaluation Institute of Industrial Technology (KEIT) and the Ministry of Trade, Industry & Energy (MOTIE, Korea) of the Republic of Korea (No. RS-2023-00262421).

**Data availability** All data included in this study are available upon request by contact with the corresponding author on reasonable request.

## References

1. K. Bae, K.S. Go, W. Kim, D. Lee, *Korean Chem. Eng. Res.* **135**, 61–61 (2023)
2. L.M. Esteves, H.A. Oliveira, F.B. Passos, *J. Ind. Eng. Chem.* **65**, 1–12 (2018)
3. M.J. Lee, S. Kim, S.W. Kim, *Int. J. Heat Mass Transf.* **204**, 123858 (2023)
4. L. Mleczko, *Ind. Eng. Chem. Res.* **58**, 21173 (2019)
5. S.Y. Son, D.H. Lee, S.D. Kim, S.W. Sung, Y.S. Park, J.H. Han, *Korean J. Chem. Eng.* **23**, 838 (2006)
6. H. Yu, Q. Zhang, G. Gu, Y. Wang, G. Luo, F. Wei, *AIChE J.* **52**, 4110 (2006)
7. S.W. Kim, *Processes* **6**, 121 (2018)
8. Y. Wang, F. Wei, G. Gu, H. Yu, *Physica B Condens. Matter.* **323**, 327 (2002)
9. S.W. Kim, *Korean Chem. Eng. Res.* **55**, 646 (2017)
10. S. Vashisth, A.A. Motlagh, S. Tebianian, M. Salcudean, J.R. Grace, *Chem. Eng. Sci.* **134**, 269 (2015)
11. W. Shuai, L. Huang, G. Jianmin, L. Huilin, L. Guodong, X. Pengfei, H. Yurong, *Appl. Math. Model.* **37**, 8179 (2013)
12. J. Xie, W. Zhong, A. Yu, *Adv. Powder Technol.* **29**, 2859 (2018)
13. J.C. Bandara, C. Jayarathna, R. Thapa, H.K. Nielsen, B.M. Moldestad, M.S. Eikeland, *Chem. Eng. Sci.* **227**, 115917 (2020)
14. M.J. Lee, S.W. Kim, *Materials* **12**, 2035 (2019)
15. J.H. Lim, D.H. Lee, *Korean Chem. Eng. Res.* **55**, 698 (2017)
16. H. Liu, R.J. Cattolica, R. Seiser, *Chem. Eng. Sci.* **169**, 235 (2017)

17. J.H. Lim, K. Bae, J.H. Shin, J.H. Kim, D.H. Lee, J.H. Han, D.H. Lee, *Powder Technol.* **288**, 315 (2016)
18. E.S. Go, S.Y. Kang, S.B. Seo, H.W. Kim, S.H. Lee, *Korean Chem. Eng. Res.* **58**, 651 (2020)
19. S. Kim, G. Won, M.J. Lee, S.W. Kim, *Korean Chem. Eng. Res.* **60**, 535 (2022)
20. M.J. Andrews, P.J. O'Rourke, *Int. J. Multiph. Flow* **22**, 379 (1996)
21. H. Zhang, Y. Lu, *Particuology* **49**, 134 (2020)
22. N. Yang, W. Wang, W. Ge, J. Li, *Chem. Eng. J.* **96**, 71 (2003)
23. L.W. Rong, K.J. Dong, A.B. Yu, *Chem. Eng. Sci.* **116**, 508 (2014)
24. D. Gidaspow, *Lattice-Boltzmann simulation of fluid flow through packed beds of spheres: Effect of particle size distribution* (Academic Press Inc, London, 1993)
25. J.F. Richardson, *Fluidization* **2**, 25 (1971)
26. R.P. Chhabra, L. Agarwal, N.K. Sinha, *Powder technol.* **101**, 288 (1999)
27. C.Y. Wen, *Chem. Eng. Progress. Symposium Series* **62**, 100 (1966)
28. S. Ergun, *Chem. Eng. Prog.* **48**, 89 (1952)
29. C.K. Jayarathna, M. Balfe, B.E. Moldestad, L.A. Tokheim, *Processes* **10**, 1855 (2022)
30. J.C. Bandara, R. Thapa, H.K. Nielsen, B.M.E. Moldestad, M.S. Eikeland, *Part. Sci. Technol.* **39**, 223 (2021)
31. Y. Go, S. Kim, Y.J. Chang, G. Won, S.W. Kim, *Renew. Energ.* **228**, 120658 (2024)
32. Z. Peng, E. Doroodchi, G.M. Evans, *Powder Technol.* **223**, 3 (2012)
33. C.E. Yeo, S.W. Kim, *Adv. Powder Technol.* **31**, 1946 (2020)
34. S.W. Kim, S.D. Kim, *Processes* **6**, 80 (2018)
35. S.W. Jeong, J.H. Lee, J. Kim, D.H. Lee, *J. Ind. Eng. Chem.* **35**, 217 (2016)
36. H.T. Bi, *Chem. Eng. Sci.* **62**, 3473 (2007)
37. H. Taofeeq, M. Al-Dahhan, *Chem. Eng. Res. Des.* **138**, 87 (2018)
38. S.K. Kim, *Korean Chem. Eng. Res.* **57**, 105 (2019)

**Publisher's Note** Springer Nature remains neutral with regard to jurisdictional claims in published maps and institutional affiliations.

Springer Nature or its licensor (e.g. a society or other partner) holds exclusive rights to this article under a publishing agreement with the author(s) or other rightsholder(s); author self-archiving of the accepted manuscript version of this article is solely governed by the terms of such publishing agreement and applicable law.